

Accelerating the prediction of stacking fault energy by combining *ab initio* calculations and machine learning

Albert Linda,¹ Md. Faiz Akhtar,¹ Shaswat Pathak,² and Somnath Bhowmick^{1,*}

¹*Department of Materials Science and Engineering,
Indian Institute of Technology Kanpur, Kanpur 208016, India*

²*Department of Mechanical Engineering, SRM College of Engineering And Technology, Kattankulathur-Chennai, 603203, India*
(Dated: May 9, 2024)

Stacking fault energies (SFEs) are key parameters to understand the deformation mechanisms in metals and alloys, and prior knowledge of SFEs from *ab initio* calculations is crucial for alloy designing. Machine learning (ML) algorithms used in the present work show a ~ 80 times acceleration of generalized stacking fault energy (GSFE) predictions, which are otherwise computationally very expensive to get directly from density functional theory (DFT) calculations, particularly for alloys. The origin of the features used for training the ML algorithms lies in the physics-based Friedel model, and the present work uncovers the connection between the physics of d-electrons and the deformation behavior of transition metals and alloys. Predictions based on the ML model agree with the experimental data. Our model can be helpful in accelerated alloy designing by providing a fast method of screening materials in terms of stacking fault energies.

I. INTRODUCTION

Stacking fault (SF) in face-centered cubic (FCC) materials is a planar defect that arises during plastic deformation through dissociating a perfect dislocation into two Shockley partial dislocations. Stacking fault energy (SFE) is a crucial parameter that determines the deformation mechanisms of FCC materials. Materials with low-to-medium SFE generally deform via transformation-induced plasticity (TRIP) or twinning-induced plasticity (TWIP), while those with high SFE deform via dislocation slip. SFE depends on several parameters like temperature [1, 2] and stress [3, 4] and it can be tuned via alloying [5–8]. Since SFE dictates dislocation dissociation, it is one of the determining factors for the dislocation pile-up at the twin boundaries (TBs), resulting in fatigue cracking [9]. Deformation processing (like ball milling, rolling, and torsion) or lattice mismatch-induced interface strain can form high-density SFs in low-to-medium SFE metals, leading to strain hardening while maintaining good ductility [10]. SFE plays a major role in the mechanical properties of bulk nanostructured materials processed via severe plastic deformation [11]. The creep life of Ni-based superalloys improves due to SFE reduction by alloying with Co [12]. Due to its importance in the mechanical behavior of metals, several experimental and computational methods have been developed for SFE estimation, as discussed below.

Experimentally, SFEs are estimated by transmission electron microscopy (TEM) or by X-ray diffraction (XRD) and neutron diffraction (ND). Using TEM, the intrinsic SFE is estimated by measuring the stacking fault width, which is defined as the separation distance of isolated pairs of leading and trailing partial dislocations. This method assumes a balance between the excess en-

ergy stored in the stacking fault and the elastic strain energy responsible for the mutual repulsion of leading and trailing partials [13]. The determination of SFE through XRD and ND involves analyzing the shift and broadening of the Bragg peak, considering the relationship between stacking fault probability, dislocation density, and intrinsic SFE [14]. An *in situ* XRD method to measure the critical stress in the early stage of plastic deformation provides another way of estimating SFE experimentally [15, 16].

The experimental methods mentioned above have one limitation - SFE at any unstable point (lying between perfect and faulted crystal) cannot be estimated. Such curves with SFE values at multiple points between perfect and faulted crystals are known as the generalized stacking fault energy (GSFE) profile or γ surface. Computational methods like DFT or classical molecular dynamics (MD) are used to calculate the γ surface [4, 17–21]. The γ surface represents the potential energy landscape between adjacent planes in a slip system. Simulated γ surface acts as an input for calculating the Peierls stresses via the Peierls-Nabarro model (P-N model) for studying dislocations [22–30], plastic deformation in high entropy alloys [31, 32] and phase transitions [33, 34]. Due to its *ab initio* nature, γ surface predicted by DFT is believed to be very accurate, and the SFE values are in reasonable agreement with experimental findings. However, DFT calculation predicts negative SFEs for some materials like metastable alloys, which are experimentally reported to have small but positive SFE [35–41]. Several attempts have been made to understand the reasons behind the discrepancy, further establishing the reliability of DFT for SFE prediction [14, 42].

Accuracy and reliability of DFT for SFE prediction lies in its ability to accurately incorporate the effect of electronic contributions [43–49]. For example, I. R. Harris et al. showed the connection between the electronic structure (empty d-states) and SFE [50]. Datta et al. found that the electronic density of states (DOS) plots

* bsomnath@iitk.ac.in

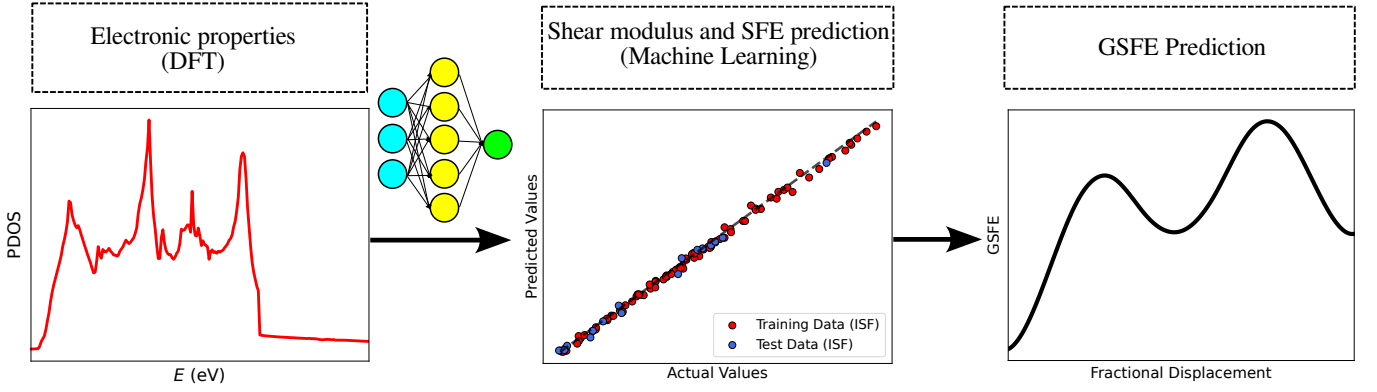


FIG. 1. Workflow for physics based accelerated generalized stacking fault energy (GSFE) calculation: *ab initio* electronic density of states (DOS) calculation, followed by machine learning based prediction of stacking fault energy and GSFE curve.

for the faulted structures are considerably smoother compared to the pristine materials [51]. A study on the influence of solute substitutions in Ni on its GSFE found a correlation between density of state (DOS) and intrinsic stacking fault (ISF) energy [52]. The energy barriers for both deformation slip and twinning formation decrease with the increased electron concentrations in ZnS, ZnTe, and CdTe [53]. A recent study also revealed a direct correlation of SFE with the width of the d-band of FCC transition metals [4]. As suggested by the previous studies, a deep connection exists between the electronic band structure and SFE, which we would like to explore in detail in the present work.

In contemporary times, machine learning (ML) algorithms have emerged as practical tools capable of achieving robust predictive outcomes for a given input dataset. Recent reports highlight the application of ML in several domains of materials science and engineering, like potential development [54], microstructure modeling [55], and structure-property correlation [56, 57]. In alloy development, ML has been employed for predicting phase stability, glass forming ability, and properties as a function of alloy composition [58–60]. Stacking fault energy, the subject matter of this paper has also been predicted using ML models using local composition, atomic size, electronic structure, physical, thermomechanical, and elastic properties as descriptors [61–66]. However, it is noteworthy that the values of these fundamental properties for alloys are often estimated using the rule of mixture, introducing potential discrepancies in the results. A few studies have attempted to predict SFE using charge density obtained from DFT calculations [67, 68].

The novelty of the present work lies in its use of the physics-based Friedel model for deriving the features for machine learning. The physics-based model helps us to uncover the connection between the SFE and electronic band structure of FCC transition metals and alloys. A schematic diagram is illustrated in Figure 1. First, we calculate the electronic density of states (DOS), a routine job for DFT packages. Using the electronic DOS data, we calculate some parameters like the width of the

d-band (W_d), energy at the band center (ε_d), electrons in the d-orbital (z_d), and electrons in the s-orbital (z_s). Using various machine learning models [Gaussian process regression (GPR), support vector regression (SVR), deep neural network (DNN), and random forest], we are able to predict the stacking fault energy and shear modulus of transition metals and alloys using the parameters obtained from DOS. Values predicted by the ML models agree with the experimental data. We are also able to predict the GSFE curve with reasonable accuracy, and our combined *ab initio*-ML approach can accelerate the GSFE calculation 80x faster compared to solely *ab initio* based approach in the case of alloys. Our work paves the way for fast and accurate computational prediction of transition metal alloys with desired SFE values, providing a valuable understanding of the deformation mechanism and mechanical behavior.

II. METHODOLOGY

Density functional theory (DFT) calculations, as implemented in the Vienna Ab-initio Simulation Package (VASP) [69], are performed using a plane wave basis set (with a 400 eV kinetic energy cut-off) and projector augmented wave (PAW) potentials [70]. The generalized gradient approximation (GGA), applying Perdew, Burke, and Ernzerhof (PBE) as exchange-correlation functional [71], is used. The unit cell parameters and atomic coordinates are fully relaxed until the energy converges to within 10^{-6} eV and the atomic force dips below 0.01 eV/Å. Further details about the supercell size and k-point mesh used for Brillouin zone sampling are given in the respective sections.

TABLE I. Comparison of SFEs obtained from DFT using two approaches (supercell and ANNNI model), predicted SFEs (using deep neural network or DNN) and experimental data [72]^a, [73]^b, [74]^c. A similar comparison for shear modulus values obtained through DFT, predicted using DNN and experimental values [75]^d. Both DFT and ML-predicted values are in good agreement with the experimental values.

Metals	DFT					Predicted			Exp.	
	Supercell		ANNNI		G	γ_{ISF}	γ_{ESF}	G	γ_{ISF}	G ^d
	γ_{ISF}	γ_{ESF}	γ_{ISF}	γ_{ESF}						
Ag	16.9	16.3	17.5	18.4	22.0	18.1	23.2	22.8	25.0 ^a	27.0
Au	32.6	31.7	23.6	23.3	15.4	32.8	37.5	19.2	45.0 ^a	27.7
Cu	42.4	44.6	48.7	53.3	49.8	43.8	56.3	39.6	55.0 ^b	48.3
Ir	357.2	333.1	348.3	334.3	214.4	359.6	400.3	216.1	480.0 ^c	210.0
Ni	136.6	133.9	140.8	135.0	95.1	138.5	162.7	95.1	125.0 ^c	75.0
Pd	139.5	134.3	146.6	139.5	44.4	137.1	148.3	45.1	130.0 ^a	43.6
Pt	309.1	299.5	277.0	282.6	48.6	299.8	315.6	50.6	322.0 ^c	61.0
Rh	203.4	194.3	190.2	188.2	146.8	207.0	240.4	150.5	330.0 ^a	150.0
Pd-Pt	190.8	180.9	176.0	172.0	45.8	172.2	186.5	47.0	-	-
Ir-Pt	359.5	342.9	328.5	326.2	163.5	326.6	371.5	150.5	-	-
Pd-Au	131.4	128.2	118.0	112.0	37.4	116.0	123.9	37.5	-	-

III. RESULTS AND DISCUSSION

A. Stacking fault energy calculations

1. SFE using periodic supercell

We consider an ideal FCC structure composed of 9 layers stacked in an ...ABCABACABC... pattern [Figure 2(a)]. Two of the cell vectors, $\frac{1}{2}[\bar{1}10]$ and $\frac{1}{2}[\bar{1}01]$, lie on the (111) plane, while the third one is perpendicular to the (111) plane and aligned along the $[111]$ direction. An intrinsic stacking fault (ISF) has a stacking sequence of ...ABCABACABC..., as shown in Figure 2(a).

An ISF is created by fixing the bottom five layers and displacing each of the top four layers by the Burgers vector $\vec{b} = \frac{1}{6}[\bar{2}11]$. Simultaneously, we shift the out-of-the-plane cell vector (oriented initially along the $[111]$ direction) by the same vector \vec{b} to preserve the unit cell's periodicity. This approach enables us to compute the stacking fault energy using periodic cells, eliminating the need for introducing surface layers [76]. We define the intrinsic stacking fault energy γ_{ISF} as the energy difference between the faulted and ideal structures per unit area:

$$\gamma_{ISF} = \frac{E_{ISF} - E_{FCC}}{A}. \quad (1)$$

To get the energy values for metals from DFT calculations, we use $21 \times 21 \times 2$ k-point mesh.

An extrinsic stacking fault (ESF) has a stacking sequence of ...ABCABACABC..., as shown in Figure 2(a). Starting with the ISF structure, we now fix the bottom six layers and displace the top three layers by $\vec{b} = \frac{1}{6}[\bar{2}11]$. The out-of-the-plane cell vector is also shifted by \vec{b} , yielding the ESF stacking sequence [Figure 2(a)]. Notably, in the case of ESF, the top 3 layers and the out-of-the-plane cell vector are displaced by $2\vec{b}$ relative to the ideal FCC configuration. To determine the γ_{ESF} value, we employ an expression similar to Equation 1.

Apart from the γ_{ISF} and γ_{ESF} , we compute stacking fault energies at various displacements, ranging from 0 to $2b$, with a step size of $0.1b$ to delineate the entire GSFE curve, as shown in Figure 3. Two significant peaks along the GSFE curve are noteworthy—one situated at approximately the middle of ideal FCC and ISF (referred to as the unstable stacking fault or USF), and the other located at approximately the middle of ISF and ESF (referred to as the unstable twinning fault or UTF). These peaks represent the energy barriers for forming ISF and ESF, respectively.

We illustrate the GSFE curves of all the transition and noble metals having FCC ground state in Figure 3. The symbols in the figure represent the values calculated from DFT. The curves are drawn using the following expressions:

$$\gamma = \begin{cases} cG \sin^2(\pi x) + \gamma_{ISF} \cdot x, & 0 \leq x \leq 1 \\ cG \sin^2(\pi x) + \gamma_{ISF} \cdot (2 - x) + \gamma_{ESF} \cdot (x - 1), & 1 \leq x \leq 2 \end{cases} \quad (2)$$

where γ_{ISF} , γ_{ESF} and shear modulus G are calculated

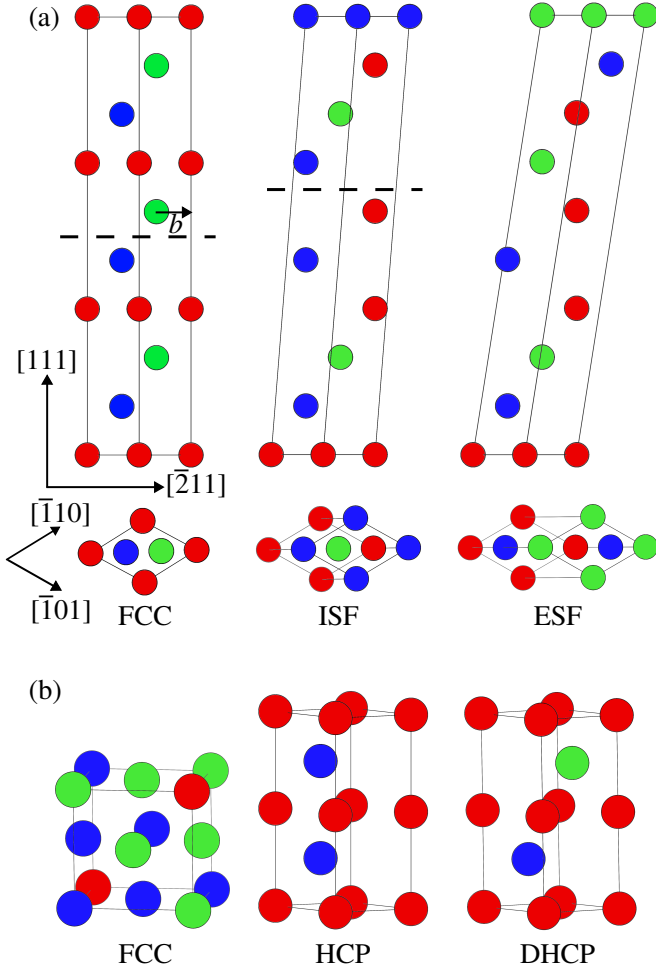


FIG. 2. (a) Supercell method: side view (first row) and top view (second row) of the supercell of the face centered cubic or FCC (left), intrinsic stacking fault or ISF (center) and extrinsic stacking fault or ESF (right). Starting from the FCC structure, all the atoms located above the dotted line and the out-of-plane cell vector are displaced by \vec{b} ($2\vec{b}$) to go from the FCC to ISF (ESF) structure. (b) ANNNI model: FCC, hexagonal closed packed or HCP and double hexagonal closed packed or DHCP cells used for the stacking fault energy calculations. In both (a) and (b) the A, B and C stacking sequence of atoms along the closed packed direction are represented in red, blue and green colors respectively.

from DFT, c is a constant, and x is the fractional displacement in terms of Burgers vector \vec{b} . The values of c are 5.01 for Ag, 5.67 for Au, 3.43 for Cu, 3.74 for Pd, 2.96 for Pt, 2.61 for Ni, 3.04 for Rh, and 2.81 for Ir. We calculate the shear modulus via strain-energy approach [77] by using VASPKIT tool [78], details of which are given in Section I, Supplemental Material (SM) [79]. In conclusion, one can generate the entire GSFE curve with reasonable accuracy by calculating three numbers: γ_{ISF} , γ_{ESF} , and G from DFT. Such an approach is computationally cheaper than calculating the entire GSFE curve from DFT, particularly when dealing with alloys.

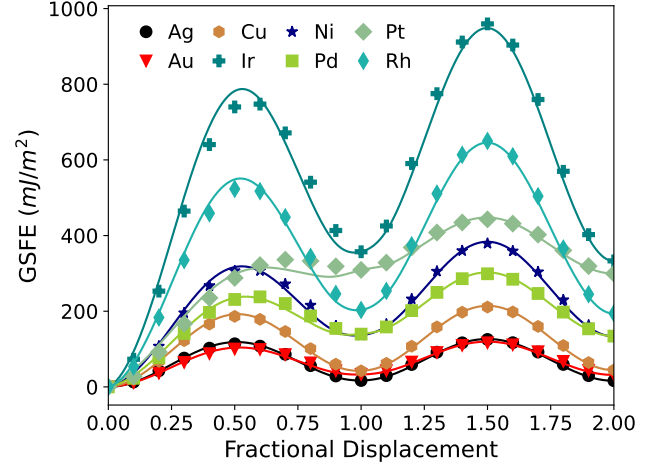


FIG. 3. Generalized stacking fault energy (GSFE) curves for FCC metals, illustrated along the $[\bar{2}11]$ direction. Energy values are plotted from 0 to $2\vec{b}$, where Burgers vector $\vec{b} = \frac{1}{6}[\bar{2}11]$. Symbols depict DFT values, while the curves are fitted using Equation 2.

2. SFE using ANNNI model

Axial-next-nearest-neighbor using (ANNNI) model is an alternate route for finding SFEs. Although the model is computationally less expensive, one can get only the ISF and ESF values instead of the entire GSFE curve. ANNNI model uses specific combinations of energies corresponding to different short-period stacking sequences of close-packed (111) planes. For example, the second-order approximation to obtain the ISF and ESF energies is given by the following combinations:

$$E_{ISF} = \frac{E_{HCP} + 2E_{DHCP} - 3E_{FCC}}{A}, \quad (3)$$

$$E_{ESF} = \frac{4(E_{DHCP} - E_{FCC})}{A}.$$

In the above equation, $A = \frac{\sqrt{3}}{4}a^2$, where a is the lattice parameter of a conventional FCC unit cell. Energies of the face-centered cubic (ABCABC stacking), hexagonal close-packed (ABAB stacking), and double hexagonal close-packed (ABACABAC stacking) structures are denoted by E_{FCC} , E_{HCP} , and E_{DHCP} , respectively. FCC, HCP, and DHCP unit cells used for the SFE calculation using the ANNNI model are illustrated in Figure 2(b). To get the energy values for metals from DFT calculations, we use $12 \times 12 \times 12$, $21 \times 21 \times 5$, and $21 \times 21 \times 5$ k-point mesh for FCC, HCP, and DHCP, respectively. SFE values calculated from the supercell method and ANNNI model are compared in Table I. Besides Au, values obtained from both models are in remarkable agreement.

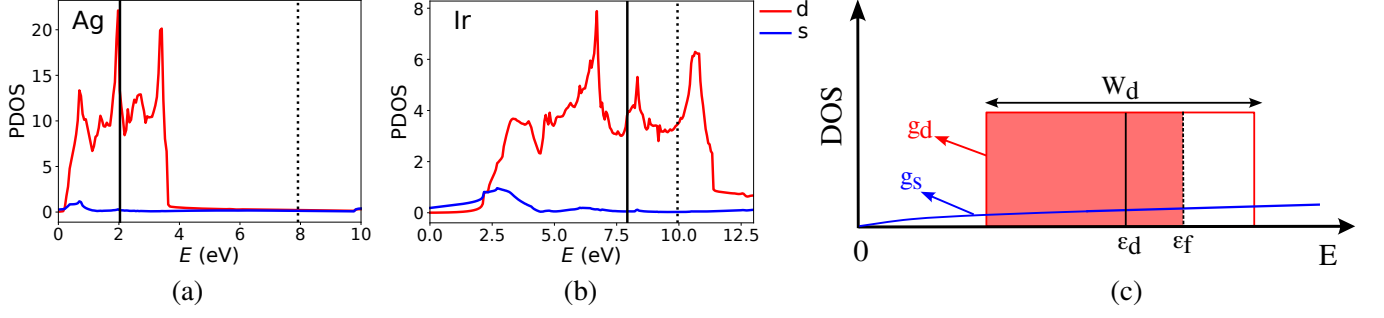


FIG. 4. Orbital projected density of states for (a) Ag (completely full narrow d-band, low SFE) and (b) Ir (partially full wide d-band, high SFE). The black solid line denotes the d-band center (ϵ_d), while the dotted line represents the Fermi energy (E_F). (c) Schematic s-band and d-band electronic density of states, according to the Friedel model.

B. Friedel model

Understanding electronic structure is the primary building block for a comprehensive study of the material's properties. Electrons serve as the quantum glue that keeps the nuclei of a solid together and influences the mechanical, electrical, optical, and magnetic properties of materials. It is well known that d-electrons play a significant role in transition metals' electronic and magnetic properties. Figures 4(a)-(b) illustrate the DOS of s-electrons and d-electrons of Ag and Ir, respectively. Unlike the DOS of s-states, the DOS of d-states is sharply peaked, which indicates that d-states are relatively localized compared to the s-states. Although the DOS curves are quite intricate, Friedel proposed a significant simplification. The DOS of s-states, denoted by $g_s(\epsilon)$, is approximated to be free electron like, obeying $g_s(\epsilon) \propto \sqrt{\epsilon}$ [Figure 4(c)]. The DOS of d-states, denoted by $g_d(\epsilon)$, is approximated to be a step function [Figure 4(c)], expressed as,

$$g_d(\epsilon) = \frac{10}{W_d}, \quad \epsilon_d - \frac{W_d}{2} < \epsilon < \epsilon_d + \frac{W_d}{2} \quad (4)$$

$$= 0, \quad \text{otherwise.}$$

The center of the d-band and its width are denoted by ϵ_d and W_d , which are related to the projected density of states (PDOS) of the d-band. The first moment of DOS with respect to the Fermi energy (ϵ_F) is,

$$\mu = \int (\epsilon - \epsilon_F) g_d^{DFT}(\epsilon) d\epsilon, \quad (5)$$

where $g_d^{DFT}(\epsilon)$ is the PDOS of d-band, obtained from the *ab initio* calculations. The number $\epsilon_d = (\epsilon_F - |\mu|)$ corresponds to the center of the d-band. Further, we calculate the second moment of the DOS with respect to ϵ_d ,

$$\sigma^2 = \int (\epsilon - \epsilon_d)^2 g_d^{DFT}(\epsilon) d\epsilon. \quad (6)$$

We define the width of the d-band as $W_d = 2\sigma$. As shown in Figure S1 and S2 in SM, the periodic trend of calculated ϵ_d and W_d agree with the solid-state table [80].

It is evident that, unlike s-states, d-states can not be treated using free electron theory, and a tight binding-like description would be more appropriate. In a tight binding description, bandwidth is an important parameter that depends on the overlap of atomic orbitals. For example, core states have zero width because of no overlap. Valence d-states have a finite width, leading to some energy gain, depending on W_d . Using the DOS expression in Equation 4, one can illustrate that the energy gain is,

$$E_d = 5W_d \left[-\frac{z_d}{10} + \left(\frac{z_d}{10} \right)^2 \right], \quad (7)$$

where z_d is the number of electrons in the d-band. We compute z_d from the *ab initio* calculations by integrating the d-band PDOS up to the Fermi energy. We obtain W_d from *ab initio* calculations using Equation 6. We define E_d as the cohesive energy due to the overlap of adjacent d-bands. The term within the square bracket in Equation 7 has a minimum at $z_d = 5$ (middle of the transition metal series), and it is zero at $z_d = 10$ (noble metal). Our *ab initio* calculations confirm that z_d increases as we move from left to right of a row in the periodic table [Figure S3 in SM]. However, z_d is slightly less than 10 in noble metals, as some electrons are transferred to the free electron-like band. Interestingly, we also find a periodic trend in W_d along a particular row; values increase from the left to the center and decrease from the center to the noble metal. In other words, W_d has a maximum near the middle of the transition metal series [Figure S2 in SM]. According to the Friedel model, the binding energy [Equation 7] of transition metals is maximum near the middle of a row [Figure S4 in SM]. This trend is in reasonably good agreement with experimental values. For example, the melting point is higher near the middle of the transition metal series [Figure S4 in SM]. Such a correlation makes the Friedel model credible despite its simplicity.

We calculate the Wigner-Seitz radius r_0 by equating volume per atom (obtained from *ab initio*) to $4\pi r_0^3/3$. Values of r_0 obtained from *ab initio* agree well with the ones reported in the solid state table [Figure S5, SM].

Since d-band overlap decreases with increasing distance between the atoms, we assume bandwidth $W_d \propto r_0^{-\alpha}$. As a result, volume dependence of E_d , denoted by κ_d , can be expressed as,

$$\kappa_d = \frac{\partial E_d}{\partial r_0} = \frac{5\alpha W_d}{r_0} \left[\frac{z_d}{10} - \left(\frac{z_d}{10} \right)^2 \right]. \quad (8)$$

Similar to E_d , κ_d also peaks near the middle of the transition metal series [Figure S6, SM].

In summary, the Friedel model defines binding among d-electrons in terms of specific material parameters, which can be computed from the electronic density of states obtained from *ab initio* calculations. In the following section, we use these parameters to fit a machine learning model, which can predict SFE values of transition metals and binary alloys.

C. Machine learning

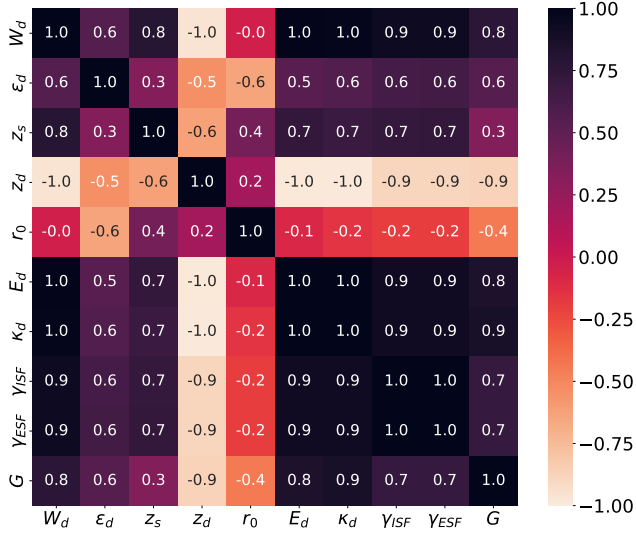


FIG. 5. Heatmap of Pearson correlation coefficient matrix: target variables are γ_{ISF} , γ_{ESF} , G and feature variables are W_d , ϵ_d , z_s , z_d , r_0 , E_d , κ_d . Values close to black (white) indicate strongly positive (negative) correlations.

1. Data generation using ANNNI model

We use the ANNNI model to generate an extensive database of γ_{ISF} and γ_{ESF} values for Au-Pd, Pd-Ag, Ag-Au, Rh-Pd, Ir-Pd, Pd-Pt, Cu-Pt, Ir-Pt, Ni-Ag, Ni-Au, Ni-Pd, Ni-Pt, Ni-Rh and Ni-Cu binary alloys. These alloys are selected because of the solid solubility of the two elements throughout the composition range, spanning from 12.5% to 87.5%, with intervals of 12.5%, encompassing seven compositions for each alloy. Using the ATAT package [81], we generate special quasirandom

structures (SQS) to describe the random arrangement of constituent atoms in a binary alloy. We generate three types of supercells, each containing 32 atoms: a conventional $2 \times 2 \times 2$ FCC supercell, a $2 \times 2 \times 4$ HCP supercell, and a $2 \times 2 \times 2$ DHCP supercell. We use a k-point mesh of $12 \times 12 \times 12$ for FCC, $21 \times 21 \times 5$ for HCP and DHCP supercell. The complete dataset for training and testing the ML model contains γ_{ISF} , γ_{ESF} and G values for 8 metals and all the binary alloys mentioned above. We also calculate the d-band PDOS and related parameters [Figure 4(c)] using the FCC supercell of the metals and alloys.

2. Feature and model selection

We aim to train a model to predict γ_{ISF} , γ_{ESF} and G of a material from its DOS, such that one can generate the GSFE curves using Equation 2. For the purpose of prediction, we use ϵ_d , W_d , z_d , r_0 , and z_s (number of s-electrons) as feature variables. Except r_0 , the rest of the features have moderate to high values of correlation coefficients [Figure 5]. Notably, z_d (number of d-electrons) has a very high negative correlation with SFEs, which implies lower SFE for a material with higher z_d . This observation agrees with the experimental facts that noble metals (Au, Ag, Cu) have low SFEs, as they have the highest d-electrons. Bandwidth W_d has a very high positive correlation with SFEs, which is again consistent with the fact that noble metals have narrow bands compared to others [Figure 4 and Figure S7, S8 in SM], resulting in low SFEs.

Although some features have high correlation coefficients, a multivariable linear regression fails to predict the target variables accurately. Thus, we use other regression methods like deep neural network (DNN), support vector regression (SVR), Gaussian process regression (GPR), and random forest. We split the data set for training and testing (80:20). The latter is used to test the trained model and compute the test error. The mean absolute error between the actual and predicted values gives the loss. We select the model that exhibits the highest coefficient of determination for total average R^2 for the test set and the highest total R^2 for the training set as the optimal one for each approach. The following discussion covers DNN and random forest, while SVR and GPR are given in Section II and Figure S9, SM.

3. Deep neural network

DNNs can capture highly non-linear relationships and complex patterns because of their highly flexible and expressive interconnected architecture [82]. We evaluate the performance of different activation functions, like rectified linear unit (ReLU), leaky ReLU, and parametric ReLU (PReLU). PReLU demonstrates superior overall performance, achieving the highest accuracy among

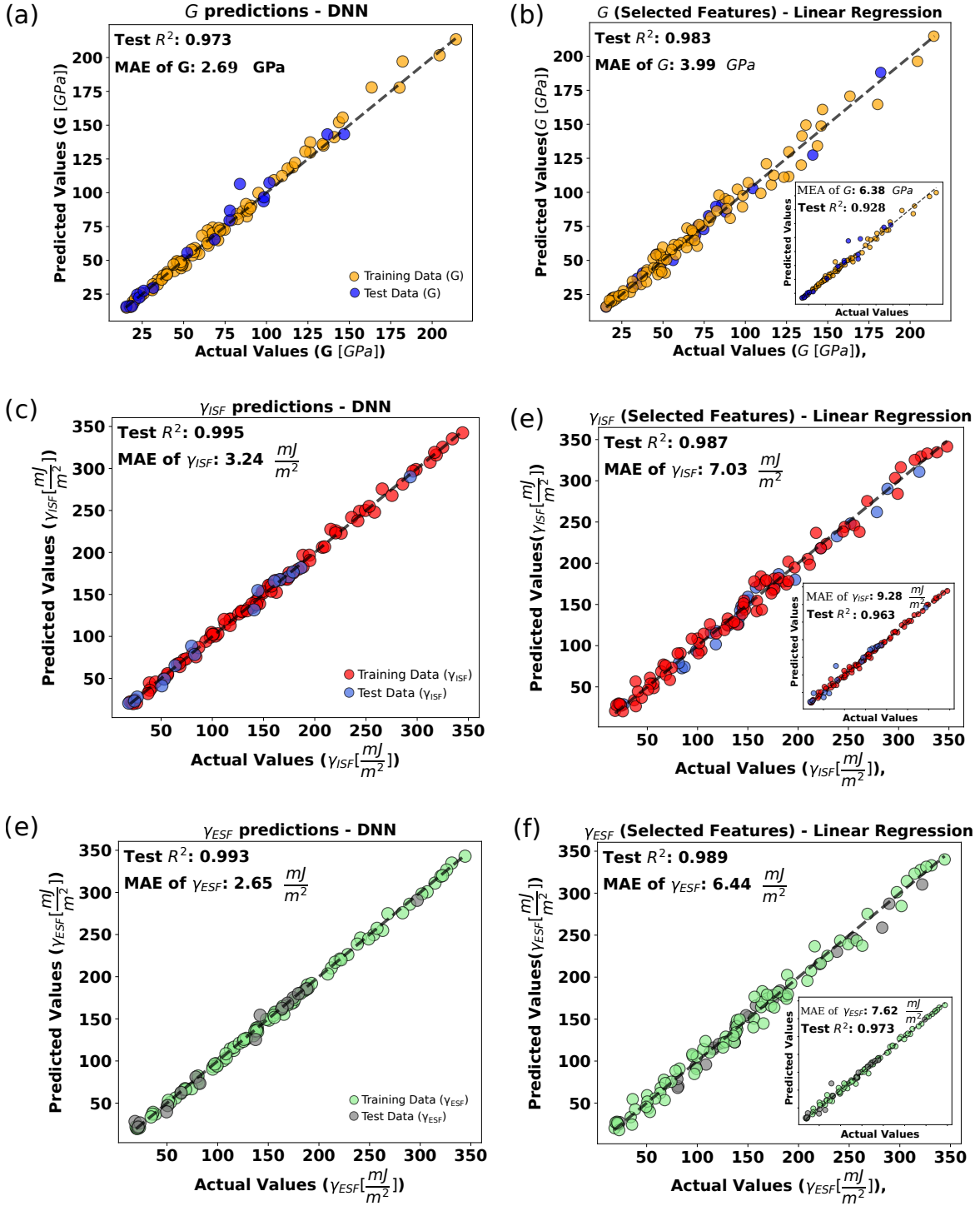


FIG. 6. Panels (a), (c) and (e) illustrate the comparison between actual and predicted values from DNNs for G , γ_{ISF} and γ_{ESF} , respectively. Panels (b), (d), and (f) depict the same for selected features using Equations 9, 10 and 11, while the insets illustrate the outcomes of random forest regression with all the features.

the tested activation functions with a test R^2 of 0.995 for γ_{ISF} prediction, compared to leaky ReLU (0.993) and traditional ReLU (0.988). The neural network with PReLU activation showcases enhanced resistance to sam-

ple bias because of its adaptive nature to effectively modulate activation for negative inputs and minimize outliers' impact while promoting superior generalization for a more reliable and stable predictive model than leaky

ReLU and ReLU counterparts. Figure 6 (a), (c), (e) shows the predicted vs. actual values for the best models of DNN, which we train with 5-7 dense layers with a learning rate of 10^{-3} with around 200-500 epochs for iterations. We evaluate the model's performance based on the test error and the change in loss with the iterations. Convergence with the number of iterations is shown in Figure S10, SM. The test R^2 values of G , γ_{ISF} and γ_{ESF} are 0.973, 0.995 and 0.993, respectively. The mean absolute errors (MAEs) of G , γ_{ISF} and γ_{ESF} are 2.69 GPa, 3.24 mJ/m² and 2.65 mJ/m², respectively.

4. Random forest

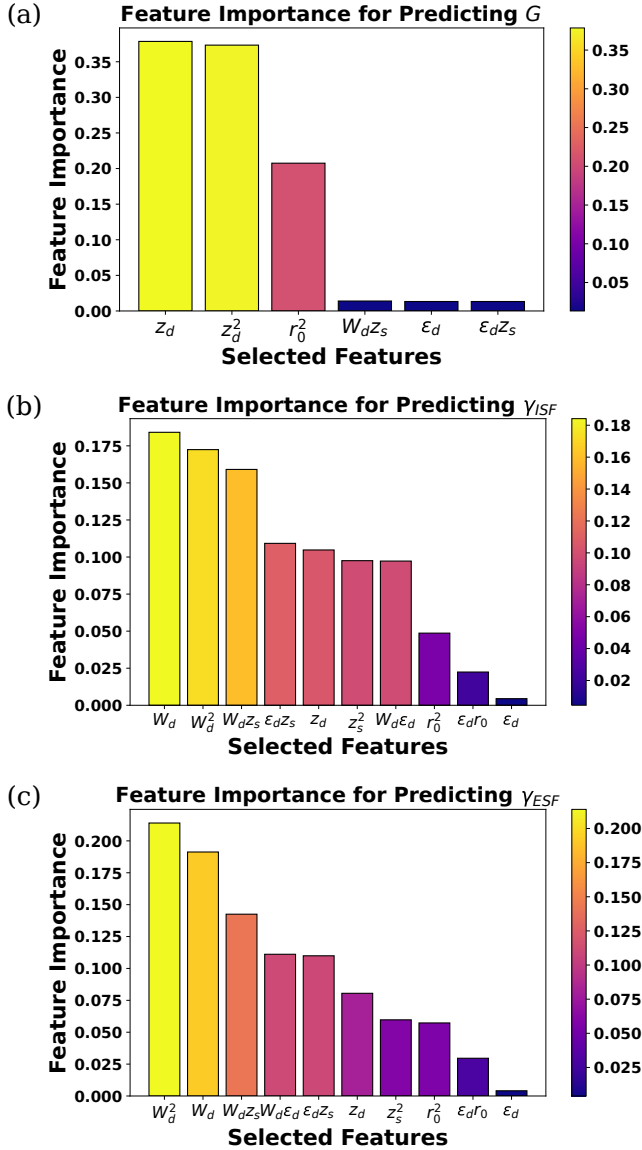


FIG. 7. Feature importance plot for G , γ_{ISF} , and γ_{ESF} .

While the DNN exhibited impressive accuracy in pre-

dicting, it is not possible to understand how γ_{ISF} , γ_{ESF} , and G depend on the feature variables. Our next objective is to predict the expression for γ_{ISF} , γ_{ESF} and G in terms of the feature variables. For this purpose, one must perform high-order polynomial regression, such as quadratic regression. This method expands the sample space from the initial five parameters (ϵ_d , W_d , z_d , r_0 , and z_s) to twenty parameters by incorporating quadratic combinations. However, employing this approach may introduce redundant parameters, potentially leading to overfitting.

A strategy to mitigate overfitting is to utilize a random forest regressor, incorporating the quadratic terms. The advantage of employing random forest lies in its ability to perform regression and simultaneously provide insights into the minimum number of terms essential for optimal prediction without the issue of overfitting by performing a search using its randomly ensembled decision trees. This process is called feature importance analysis. Details of feature importance analysis using random forest are given in Section III, SM. After feature importance analysis, we select only six terms for shear modulus prediction and ten terms for SFE prediction [Figure 7]. Finally, we do a multivariable linear regression with the selected features to obtain the following expressions, which can be directly used for prediction.

$$G = 51.07z_d^2 - 63.21r_0^2 + 25.82\epsilon_d - 876.15z_d + 33.80W_d z_s - 60.14\epsilon_d z_s + 3877.91. \quad (9)$$

$$\begin{aligned} \gamma_{ISF} = & -22.66W_d^2 - 579.36z_s^2 - 522.06r_0^2 - 220.46\epsilon_d \\ & + 27.77z_d + 64.57W_d + 18.51W_d \epsilon_d + 278.81W_d z_s \\ & - 49.31\epsilon_d z_s + 74.77\epsilon_d r_0 + 996.58. \end{aligned} \quad (10)$$

$$\begin{aligned} \gamma_{ESF} = & -21.29W_d^2 - 730.97z_s^2 - 453.58r_0^2 - 178.69\epsilon_d \\ & + 31.77z_d + 78.59W_d + 16.30W_d \epsilon_d + 249.45W_d z_s \\ & + 0.80\epsilon_d z_s + 41.06\epsilon_d r_0 + 781.64. \end{aligned} \quad (11)$$

Note that, before applying the feature importance selection analysis, the mean absolute error obtained by including all the twenty terms are 6.38 GPa, 9.28 mJ/m², and 7.62 mJ/m² for G , γ_{ISF} and γ_{ESF} [insets of Figure 6 (b), (d), (f)], which reduces to 3.99 GPa, 7.03 mJ/m², and 6.44 mJ/m² [Figure 6 (b), (d), (f)], respectively. The test R^2 values of G , γ_{ISF} and γ_{ESF} also improve from 0.928, 0.963, and 0.973 (with all twenty features) to 0.983, 0.987 and 0.989 (with selected features), respectively. The improvement can be attributed to keeping only essential features, thus reducing the problem of overfitting.

Figure 7 illustrates all the selected features that are utilized in predicting the formula [Equation 9, 10, 11] in descending order in terms of their importance. Two features are dominant for shear modulus G : linear and quadratic terms of the number of d-electrons (z_d), followed by r_0^2 . Stacking fault energies γ_{ISF} and γ_{ESF} depend on multiple features, the linear and quadratic

term of d-band width (W_d) being the most important among them. The list also contains some cross terms like $W_d\varepsilon_d$, W_dz_s , ε_dz_s with non-negligible weight, highlighting the highly non-linear nature of the problem, which requires a combined approach involving state-of-the-art *ab initio* calculations and machine learning methods for complete understanding.

D. GSFE curve prediction

So far, we have focused on training ML models for predicting γ_{ISF} , γ_{ESF} and G . Finally, we take up the most challenging task of predicting the entire GSFE. Conventionally, one should calculate the GSFE curves for several alloys using DFT and use them to train ML models. However, calculating the GSFE curves for alloys is computationally very expensive. Instead, we use the predicted G , γ_{ISF} and γ_{ESF} values from the previous section and construct the GSFE curves using Equation 2. For a binary alloy, we use the rule of mixture to get the value of c (listed after Equation 2), which is the weighted average of the pure element's values. The following discussion shows that our method makes GSFE prediction 80X faster for alloys.

Figure 8 compares the predicted GSFE curves with actual DFT values, illustrated for binary Pd-Pt, Ir-Pt, and Pd-Au alloys. We use the same technique as described earlier (Figure 2), but with a nine times larger supercell, having cell vectors $\frac{3}{2}[\bar{1}10]$, $\frac{3}{2}[\bar{1}01]$, $[111]$. Such a supercell contains eighty-one atoms, nine each in 9 different layers [Figure 8(a)]. We generate SQS to describe the random arrangement of constituent atoms in a binary alloy and use a k-point mesh of $9 \times 9 \times 3$. Because of the randomness, each layer has a different composition [Figure 8(a)], and the GSFE curve depends on the specific choice of layers during the deformation. For example, we start by fixing layer 1 and displacing layers 2 to 9, followed by fixing layers 1-2 and displacing layers 3 to 9, etc., as shown in Figure 8(a). Thus, we have to repeat the calculation eight times, and the average value yields one single DFT data point on a GSFE curve [Figure 8(b)]. The error bars show the lowest and highest among the eight DFT values calculated. Since there are 10 data points on a GSFE curve, we need to perform 80 calculations to get the entire GSFE curve from DFT directly.

Considering the large number of atoms in the supercell, predicting GSFE directly from DFT is computationally expensive for alloys. As an alternative, the pro-

posed ML approach requires only one DFT calculation to get the DOS and compute relevant parameters like ε_d , W_d , z_d , z_s , and r_0 . Using these parameters, one can predict γ_{ISF} , γ_{ESF} , and G using the ML model and finally predict the GSFE curve using Equation 2. Figure 8(b) illustrates that the ML-predicted GSFE curves are in good agreement with the actual DFT points (based on eighty DFT calculations). As shown in Figure 8(c), $\gamma_{UTF}/\gamma_{USF}$ scales linearly with $\gamma_{ISF}/\gamma_{USF}$. Predicted values agree reasonably well with the DFT results.

IV. CONCLUSIONS

In conclusion, we have proposed a combined *ab initio* and ML-based model that can accelerate the computational prediction of GSFE curves for alloys by a factor of 80. The training dataset is generated using DFT calculations to find the SFE values of 106 metals and alloys using the ANNNI model. The features used for training the ML algorithms come from the physics-based Friedel model. The features are obtained from the electronic DOS, calculated using DFT. Other than accelerating the process of GSFE calculation, the present work also highlights a deep connection between the physics of d-electrons and the deformation behavior of transition metals and alloys. Our study reveals a highly non-linear dependence of shear modulus and stacking fault energies on the electronic features, which requires a combined approach involving state-of-the-art *ab initio* calculations and machine learning methods for complete understanding. The present model can accelerate alloy designing with targeted mechanical behavior by providing a fast method of screening materials in terms of stacking fault energies.

V. ACKNOWLEDGEMENTS

We acknowledge National Super Computing Mission (NSM) for providing computing resources of "PARAM Sanganak" at IIT Kanpur, which is implemented by CDAC and supported by the Ministry of Electronics and Information Technology (MeitY) and Department of Science and Technology (DST), Government of India. We also thank ICME National Hub, IIT Kanpur and CC, IIT Kanpur for providing HPC facility.

[1] D. Molnár, X. Sun, S. Lu, W. Li, G. Engberg, and L. Vitos, Effect of temperature on the stacking fault energy and deformation behaviour in 316l austenitic stainless steel, *Materials Science and Engineering: A* **759**, 490 (2019)

[2] X. Zhang, B. Grabowski, F. Körmann, A. V. Ruban, Y. Gong, R. C. Reed, T. Hickel, and J. Neugebauer, Temperature dependence of the stacking-fault gibbs energy for al, cu, and ni, *Phys. Rev. B* **98**, 224106 (2018)

[3] P. Andric, B. Yin, and W. Curtin, Stress-dependence of generalized stacking fault energies, *Journal of the Me-*

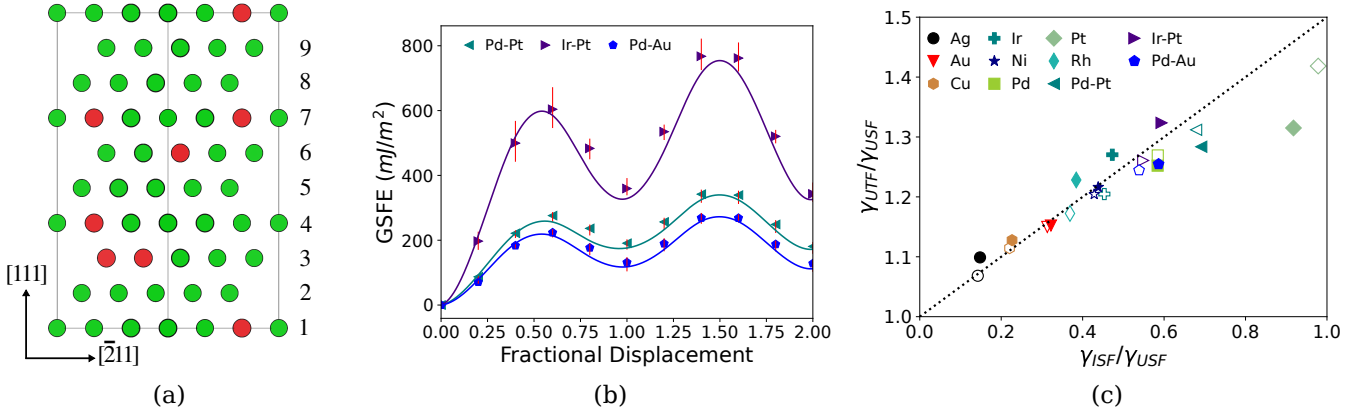


FIG. 8. (a) Supercell for GSFE calculation of alloys; numbers adjacent to the atomic planes represent the layer number. (b) GSFE curves for $\text{Pd}_{0.75}\text{Pt}_{0.25}$, $\text{Ir}_{0.75}\text{Pt}_{0.25}$, and $\text{Pd}_{0.75}\text{Au}_{0.25}$ alloys. The symbols are from DFT calculations, while the curves are generated from Equation 2, using γ_{ISF} , γ_{ESF} , and G values predicted via ML. (c) $\gamma_{UTF}/\gamma_{USF}$ scales linearly with $\gamma_{ISF}/\gamma_{USF}$, as shown by the dotted line. Comparison of actual values from DFT calculations (solid symbols) and predicted values (open symbols).

- chanics and Physics of Solids **122**, 262 (2019)
- [4] A. Linda, P. K. Tripathi, S. Nagar, and S. Bhowmick, Effect of pressure on stacking fault energy and deformation behavior of face-centered cubic metals, *Materialia* **26**, 101598 (2022)
 - [5] Q. Shao, L. Liu, T. Fan, D. Yuan, and J. Chen, Effects of solute concentration on the stacking fault energy in copper alloys at finite temperatures, *Journal of Alloys and Compounds* **726**, 601 (2017)
 - [6] J. Kumar, A. Linda, M. Sadhasivam, K. Pradeep, N. Gurao, and K. Biswas, The effect of si addition on the structure and mechanical properties of equiatomic cocrfemni high entropy alloy by experiment and simulation, *Materialia* **27**, 101707 (2023)
 - [7] Y. Zhang, J. Guo, J. Chen, C. Wu, K. S. Kormout, P. Ghosh, and Z. Zhang, On the stacking fault energy related deformation mechanism of nanocrystalline cu and cu alloys: A first-principles and tem study, *Journal of Alloys and Compounds* **776**, 807 (2019)
 - [8] S. Zhao, G. M. Stocks, and Y. Zhang, Stacking fault energies of face-centered cubic concentrated solid solution alloys, *Acta Materialia* **134**, 334 (2017)
 - [9] L. Li, Z. Zhang, P. Zhang, and Z. Zhang, A review on the fatigue cracking of twin boundaries: Crystallographic orientation and stacking fault energy, *Progress in Materials Science* **131**, 101011 (2023)
 - [10] R. Su, D. Neffati, Y. Zhang, J. Cho, J. Li, H. Wang, Y. Kulkarni, and X. Zhang, The influence of stacking faults on mechanical behavior of advanced materials, *Materials Science and Engineering: A* **803**, 140696 (2021)
 - [11] X. An, S. Wu, Z. Wang, and Z. Zhang, Significance of stacking fault energy in bulk nanostructured materials: Insights from cu and its binary alloys as model systems, *Progress in Materials Science* **101**, 1 (2019)
 - [12] C. Tian, G. Han, C. Cui, and X. Sun, Effects of stacking fault energy on the creep behaviors of ni-base superalloy, *Materials & Design* **64**, 316 (2014)
 - [13] P. Delavignette and S. Amelinckx, Dislocation patterns in graphite, *Journal of Nuclear Materials* **5**, 17 (1962)
 - [14] K. V. Werner, F. Niessen, M. Villa, and M. A. J. Somers, Experimental validation of negative stacking fault energies in metastable face-centered cubic materials, *Applied Physics Letters* **119**, 141902 (2021)
 - [15] D. Rafaja, C. Kröbetschek, C. Ullrich, and S. Martin, Stacking fault energy in austenitic steels determined by using *in situ* X-ray diffraction during bending, *Journal of Applied Crystallography* **47**, 936 (2014)
 - [16] T. Byun, On the stress dependence of partial dislocation separation and deformation microstructure in austenitic stainless steels, *Acta Materialia* **51**, 3063 (2003)
 - [17] Y. Su, S. Xu, and I. J. Beyerlein, Density functional theory calculations of generalized stacking fault energy surfaces for eight face-centered cubic transition metals, *Journal of Applied Physics* **126**, 105112 (2019)
 - [18] A. Hunter, R. F. Zhang, and I. J. Beyerlein, The core structure of dislocations and their relationship to the material γ -surface, *Journal of Applied Physics* **115**, 134314 (2014)
 - [19] Q.-M. Hu and R. Yang, Basal-plane stacking fault energy of hexagonal close-packed metals based on the ising model, *Acta Materialia* **61**, 1136 (2013)
 - [20] X.-Z. Wu, R. Wang, S.-F. Wang, and Q.-Y. Wei, Ab initio calculations of generalized-stacking-fault energy surfaces and surface energies for fcc metals, *Applied Surface Science* **256**, 6345 (2010)
 - [21] A. Jarlöv, W. Ji, Z. Zhu, Y. Tian, R. Babicheva, R. An, H. L. Seet, M. L. S. Nai, and K. Zhou, Molecular dynamics study on the strengthening mechanisms of cr-fe-co-ni high-entropy alloys based on the generalized stacking fault energy, *Journal of Alloys and Compounds* **905**, 164137 (2022)
 - [22] B. Joós, Q. Ren, and M. S. Duesbery, Peierls-nabarro model of dislocations in silicon with generalized stacking-fault restoring forces, *Phys. Rev. B* **50**, 5890 (1994)
 - [23] J. Hartford, B. von Sydow, G. Wahnström, and B. I. Lundqvist, Peierls barriers and stresses for edge dislocations in pd and al calculated from first principles, *Phys. Rev. B* **58**, 2487 (1998)

- [24] S. L. Shang, W. Y. Wang, Y. Wang, Y. Du, J. X. Zhang, A. D. Patel, and Z. K. Liu, Temperature-dependent ideal strength and stacking fault energy of fcc ni: a first-principles study of shear deformation, *Journal of Physics: Condensed Matter* **24**, 155402 (2012)
- [25] S. L. Shang, C. L. Zacherl, H. Z. Fang, Y. Wang, Y. Du, and Z. K. Liu, Effects of alloying element and temperature on the stacking fault energies of dilute ni-base superalloys, *Journal of Physics: Condensed Matter* **24**, 505403 (2012)
- [26] H. El Kadiri, J. Kapil, A. Oppedal, L. Hector, S. R. Agnew, M. Cherkaoui, and S. Vogel, The effect of twin–twin interactions on the nucleation and propagation of $101\bar{2}$ twinning in magnesium, *Acta Materialia* **61**, 3549 (2013)
- [27] A. Linda, M. F. Akhtar, and S. Bhowmick, Deformation in metals: Insights from ab-initio calculations, in *Proceedings of the International Conference on Metallurgical Engineering and Centenary Celebration*, edited by S. Patra, S. Sinha, G. S. Mahobia, and D. Kamble (Springer Nature Singapore, Singapore, 2024) pp. 83–92
- [28] Y. Kamimura, K. Edagawa, A. Iskandarov, M. Osawa, Y. Umeno, and S. Takeuchi, Peierls stresses estimated via the peierls-nabarro model using ab-initio γ -surface and their comparison with experiments, *Acta Materialia* **148**, 355 (2018)
- [29] S. Xu, J. R. Mianroodi, A. Hunter, B. Svendsen, and I. J. Beyerlein, Comparative modeling of the disregistry and peierls stress for dissociated edge and screw dislocations in al, *International Journal of Plasticity* **129**, 102689 (2020)
- [30] T. Ma, H. Kim, N. Mathew, D. J. Luscher, L. Cao, and A. Hunter, Dislocation transmission across $\sigma 3112$ incoherent twin boundary: a combined atomistic and phase-field study, *Acta Materialia* **223**, 117447 (2022)
- [31] S. Schönecker, W. Li, L. Vitos, and X. Li, Effect of strain on generalized stacking fault energies and plastic deformation modes in fcc-hcp polymorphic high-entropy alloys: A first-principles investigation, *Phys. Rev. Mater.* **5**, 075004 (2021)
- [32] L. Zhu and Z. Wu, Effects of short range ordering on the generalized stacking fault energy and deformation mechanisms in fcc multiprincipal element alloys, *Acta Materialia* **259**, 119230 (2023)
- [33] C. Yang, B. Zhang, L. Fu, Z. Wang, J. Teng, R. Shao, Z. Wu, X. Chang, J. Ding, L. Wang, and X. Han, Chemical inhomogeneity-induced profuse nanotwinning and phase transformation in aucti nanowires, *Nature Communications* **14**, 5705 (2023)
- [34] D. Wen, B. Kong, S. Wang, L. Liu, Q. Song, and Z. Yin, Mechanism of stress- and thermal-induced fct \rightarrow hcp \rightarrow fcc crystal structure change in a ti-al-based alloy compressed at elevated temperature, *Materials Science and Engineering: A* **840**, 143011 (2022)
- [35] Z. Pei, B. Dutta, F. Körmann, and M. Chen, Hidden effects of negative stacking fault energies in complex concentrated alloys, *Phys. Rev. Lett.* **126**, 255502 (2021)
- [36] K. V. Werner, F. Niessen, W. Li, S. Lu, L. Vitos, M. Villa, and M. A. Somers, Reconciling experimental and theoretical stacking fault energies in face-centered cubic materials with the experimental twinning stress, *Materialia* **27**, 101708 (2023)
- [37] D. You, O. K. Celebi, A. S. K. Mohammed, and H. Sehitoglu, Negative stacking fault energy in fcc materials: its implications, *International Journal of Plasticity* **170**, 103770 (2023)
- [38] S. Wei and C. C. Tasan, Deformation faulting in a metastable co-cu-ni complex concentrated alloy: A case of negative intrinsic stacking fault energy?, *Acta Materialia* **200**, 992 (2020)
- [39] M. Shih, J. Miao, M. Mills, and M. Ghazisaeidi, Stacking fault energy in concentrated alloys, *Nature Communications* **12**, 3590 (2021)
- [40] M. Walter, L. Mujica Roncery, S. Weber, L. Leich, and W. Theisen, Xrd measurement of stacking fault energy of cr–ni austenitic steels: influence of temperature and alloying elements, *Journal of Materials Science* **55**, 13424 (2020)
- [41] A. Chandan, S. Tripathy, B. Sen, M. Ghosh, and S. Ghosh Chowdhury, Temperature dependent deformation behavior and stacking fault energy of fe40mn40co10cr10 alloy, *Scripta Materialia* **199**, 113891 (2021)
- [42] X. Sun, S. Lu, R. Xie, X. An, W. Li, T. Zhang, C. Liang, X. Ding, Y. Wang, H. Zhang, and L. Vitos, Can experiment determine the stacking fault energy of metastable alloys?, *Materials & Design* **199**, 109396 (2021)
- [43] H. Hu, M. Zhao, X. Wu, Z. Jia, R. Wang, W. Li, and Q. Liu, The structural stability, mechanical properties and stacking fault energy of al3zr precipitates in al–cu–zr alloys: Hrtm observations and first-principles calculations, *Journal of Alloys and Compounds* **681**, 96 (2016)
- [44] S. Shi, L. Zhu, H. Zhang, Z. Sun, and R. Ahuja, Mapping the relationship among composition, stacking fault energy and ductility in nb alloys: A first-principles study, *Acta Materialia* **144**, 853 (2018)
- [45] H. Stange, S. Brunken, H. Hempel, H. Rodriguez-Alvarez, N. Schäfer, D. Greiner, A. Scheu, J. Lauche, C. A. Kaufmann, T. Unold, D. Abou-Ras, and R. Mainz, Effect of Na presence during CuInSe2 growth on stacking fault annihilation and electronic properties, *Applied Physics Letters* **107**, 152103 (2015)
- [46] W. Y. Wang, S. L. Shang, Y. Wang, Z.-G. Mei, K. A. Darling, L. J. Kecskes, S. N. Mathaudhu, X. D. Hui, and Z.-K. Liu, Effects of alloying elements on stacking fault energies and electronic structures of binary mg alloys: A first-principles study, *Materials Research Letters* **2**, 29 (2014)
- [47] X. Li, S. Schönecker, L. Vitos, and X. Li, Generalized stacking faults energies of face-centered cubic high-entropy alloys: A first-principles study, *Intermetallics* **145**, 107556 (2022)
- [48] Y. Qi and R. K. Mishra, Ab initio study of the effect of solute atoms on the stacking fault energy in aluminum, *Phys. Rev. B* **75**, 224105 (2007)
- [49] A. R. Natarajan and A. Van der Ven, Linking electronic structure calculations to generalized stacking fault energies in multicomponent alloys, *npj Computational Materials* **6**, 80 (2020)
- [50] I. Harris, I. Dillamore, R. Smallman, and B. Beeston, The influence of d-band structure on stacking-fault energy, *Philosophical magazine* **14**, 325 (1966)
- [51] A. Datta, U. Waghmare, and U. Ramamurty, Structure and stacking faults in layered mg–zn–y alloys: A first-principles study, *Acta Materialia* **56**, 2531 (2008)
- [52] K. Kumar, R. Sankarasubramanian, and U. V. Waghmare, Influence of dilute solute substitutions in ni on its generalized stacking fault energies and ductility, *Computational Materials Science* **150**, 424 (2018)

- [53] Y. Shen, H. Wang, and Q. An, Modified generalized stacking fault energy surface of ii-vi ionic crystals from excess electrons and holes, *ACS Applied Electronic Materials* **2**, 56 (2020)
- [54] Z. Li, J. R. Kermode, and A. De Vita, Molecular dynamics with on-the-fly machine learning of quantum-mechanical forces, *Phys. Rev. Lett.* **114**, 096405 (2015)
- [55] O. Ahmad, N. Kumar, R. Mukherjee, and S. Bhowmick, Accelerating microstructure modeling via machine learning: A method combining autoencoder and convlstm, *Phys. Rev. Mater.* **7**, 083802 (2023)
- [56] K. T. Schütt, H. Glawe, F. Brockherde, A. Sanna, K. R. Müller, and E. K. U. Gross, How to represent crystal structures for machine learning: Towards fast prediction of electronic properties, *Phys. Rev. B* **89**, 205118 (2014)
- [57] H. Zhang, H. Fu, X. He, C. Wang, L. Jiang, L.-Q. Chen, and J. Xie, Dramatically enhanced combination of ultimate tensile strength and electric conductivity of alloys via machine learning screening, *Acta Materialia* **200**, 803 (2020)
- [58] X. Liu, X. Li, Q. He, D. Liang, Z. Zhou, J. Ma, Y. Yang, and J. Shen, Machine learning-based glass formation prediction in multicomponent alloys, *Acta Materialia* **201**, 182 (2020)
- [59] Y. V. Krishna, U. K. Jaiswal, and R. M. R, Machine learning approach to predict new multiphase high entropy alloys, *Scripta Materialia* **197**, 113804 (2021)
- [60] V. Revi, S. Kasodariya, A. Talapatra, G. Pilania, and A. Alankar, Machine learning elastic constants of multicomponent alloys, *Computational Materials Science* **198**, 110671 (2021)
- [61] X. Chong, S.-L. Shang, A. M. Krajewski, J. D. Shimanek, W. Du, Y. Wang, J. Feng, D. Shin, A. M. Beese, and Z.-K. Liu, Correlation analysis of materials properties by machine learning: illustrated with stacking fault energy from first-principles calculations in dilute fcc-based alloys, *Journal of Physics: Condensed Matter* **33**, 295702 (2021)
- [62] S. Mahato, N. P. Gurao, and K. Biswas, Accelerated prediction of stacking fault energy in fcc medium entropy alloys using multilayer perceptron neural networks: correlation and feature analysis, *Modelling and Simulation in Materials Science and Engineering* **32**, 035021 (2024)
- [63] X. Liu, Y. Zhu, C. Wang, K. Han, L. Zhao, S. Liang, M. Huang, and Z. Li, A statistics-based study and machine-learning of stacking fault energies in heas, *Journal of Alloys and Compounds* **966**, 171547 (2023)
- [64] Y.-J. Hu, A. Sundar, S. Ogata, and L. Qi, Screening of generalized stacking fault energies, surface energies and intrinsic ductile potency of refractory multicomponent alloys, *Acta Materialia* **210**, 116800 (2021)
- [65] M. Wang, H. Yu, Y. Chen, and M. Huang, Machine learning assisted screening of non-rare-earth elements for mg alloys with low stacking fault energy, *Computational Materials Science* **196**, 110544 (2021)
- [66] T. Z. Khan, T. Kirk, G. Vazquez, P. Singh, A. Smirnov, D. D. Johnson, K. Youssef, and R. Arróyave, Towards stacking fault energy engineering in fcc high entropy alloys, *Acta Materialia* **224**, 117472 (2022)
- [67] G. Arora, A. Manzoor, and D. S. Aidhy, Charge-density based evaluation and prediction of stacking fault energies in Ni alloys from DFT and machine learning, *Journal of Applied Physics* **132**, 225104 (2022)
- [68] G. Arora, S. Kamrava, P. Tahmasebi, and D. S. Aidhy, Charge-density based convolutional neural networks for stacking fault energy prediction in concentrated alloys, *Materialia* **26**, 101620 (2022)
- [69] G. Kresse and D. Joubert, From ultrasoft pseudopotentials to the projector augmented-wave method, *Phys. Rev. B* **59**, 1758 (1999)
- [70] G. Kresse and J. Furthmüller, Efficient iterative schemes for ab-initio total energy calculations using a plane-wave basis set, *Phys. Rev. B* **54**, 11169 (1996)
- [71] J. P. Perdew, K. Burke, and M. Ernzerhof, Generalized gradient approximation made simple, *Phys. Rev. Lett.* **77**, 3865 (1996)
- [72] I. L. Dillamore and R. E. Smallman, The stacking-fault energy of f.c.c. metals, *The Philosophical Magazine: A Journal of Theoretical Experimental and Applied Physics* **12**, 191 (1965)
- [73] P. C. J. Gallagher, The influence of alloying, temperature, and related effects on the stacking fault energy, *Metallurgical Transactions* **1**, 2429 (1970)
- [74] J. P. Hirth, J. Lothe, and T. Mura, Theory of Dislocations (2nd ed.), *Journal of Applied Mechanics* **50**, 476 (1983)
- [75] A. Buch, *Short handbook of metal elements properties and elastic properties of pure metals*, 3rd ed. (Krzysztof Biesaga, 2005)
- [76] S. Kibey, J. B. Liu, D. D. Johnson, and H. Sehitoglu, Energy pathways and directionality in deformation twinning, *Applied Physics Letters* **91**, 181916 (2007)
- [77] Y. Le Page and P. Saxe, Symmetry-general least-squares extraction of elastic coefficients from ab initio total energy calculations, *Phys. Rev. B* **63**, 174103 (2001)
- [78] V. Wang, N. Xu, J.-C. Liu, G. Tang, and W.-T. Geng, Vaspkit: A user-friendly interface facilitating high-throughput computing and analysis using vasp code, *Computer Physics Communications* **267**, 108033 (2021)
- [79] See supplemental material for technical details of shear modulus calculation, materials parameters calculated from density functional theory, gaussian process regression, support vector regression, and feature importance analysis., [URLwillbeinsertedbypublisher](#).
- [80] W. A. Harrison, *Electronic structure and the properties of solids: the physics of the chemical bond* (Courier Corporation, 2012)
- [81] A. van de Walle, P. Tiwary, M. de Jong, D. Olmsted, M. Asta, A. Dick, D. Shin, Y. Wang, L.-Q. Chen, and Z.-K. Liu, Efficient stochastic generation of special quasirandom structures, *Calphad* **42**, 13 (2013)
- [82] J. Schmidhuber, Deep learning in neural networks: An overview, *Neural Networks* **61**, 85 (2015)

Accelerating the prediction of stacking fault energy by combining ab initio calculations and machine learning

Albert Linda,¹ Md. Faiz Akhtar,¹ Shaswat Pathak,² and Somnath Bhowmick^{1,*}

¹*Department of Materials Science and Engineering,
Indian Institute of Technology Kanpur, Kanpur 208016, India*

²*Department of Mechanical Engineering,
SRM College of Engineering And Technology,
Kattankulathur-Chennai, 603203, India*

(Dated: May 9, 2024)

I. ESTIMATION OF SHEAR MODULUS

Energy depends on strain via¹,

$$\Delta E(V, \varepsilon_i) = E(V, \varepsilon_i) - E(V_0) = \frac{V_0}{2} \sum_{i,j=1}^6 C_{ij} \varepsilon_j \varepsilon_i, \quad (1)$$

where $E(V, \varepsilon_i)$ and $E(V_0)$ are the energies of distorted and ideal lattice respectively. During the application of strain the lattice vectors transform like

$$\begin{bmatrix} a' \\ b' \\ c' \end{bmatrix} = \begin{bmatrix} a \\ b \\ c \end{bmatrix} (I + \epsilon). \quad (2)$$

Here, I represents the identity matrix, a, b, c and a', b', c' are the lattice vectors of the undeformed and deformed structure respectively. The above equation requires strain matrix ϵ , which is given by

$$\epsilon = \begin{bmatrix} \varepsilon_1 & \varepsilon_6/2 & \varepsilon_5/2 \\ \varepsilon_6/2 & \varepsilon_2 & \varepsilon_4/2 \\ \varepsilon_5/2 & \varepsilon_4/2 & \varepsilon_3 \end{bmatrix}. \quad (3)$$

For cubic material, three types of strain matrix is required each for estimating C_{44} , $C_{11} + C_{12}$ and $C_{11} + 2C_{12}$. The matrices are obtained by utilizing the values given in the following table.

	ε_1	ε_2	ε_3	ε_4	ε_5	ε_6
C_{44}	0	0	0	δ	δ	δ
$C_{11} + C_{12}$	δ	δ	0	0	0	0
$C_{11} + 2C_{12}$	δ	δ	δ	0	0	0

Also, we know that for cubic material the elastic stiffness matrix is given by

$$C_{ij} = \begin{bmatrix} C_{11} & C_{12} & C_{12} & 0 & 0 & 0 \\ C_{12} & C_{11} & C_{12} & 0 & 0 & 0 \\ C_{12} & C_{12} & C_{11} & 0 & 0 & 0 \\ 0 & 0 & 0 & C_{44} & 0 & 0 \\ 0 & 0 & 0 & 0 & C_{44} & 0 \\ 0 & 0 & 0 & 0 & 0 & C_{44} \end{bmatrix}. \quad (4)$$

Using C_{ij} and the strain matrix of all three cases, equation 1 change to

$$\Delta E = \frac{3}{2}C_{44}V\delta^2, \quad (5)$$

$$\Delta E = (C_{11} + C_{12})V\delta^2 \quad (6)$$

and

$$\Delta E = \frac{3}{2}(C_{11} + 2C_{12})V\delta^2. \quad (7)$$

Using above three equation we can estimate C_{11} , C_{12} and C_{44} . These values can then be used to estimate the Voigt bound for shear modulus(G). This is the upper bound², given by

$$G_V = \frac{C_{11} - C_{12} + 3C_{44}}{5}. \quad (8)$$

The Reuss bound is the lower bond³, given by

$$G_R = \frac{5}{4(S_{11} - S_{12}) + 3S_{44}}. \quad (9)$$

S_{ij} values can be obtained using the following equations,

$$S_{11} = \frac{C_{11} + C_{12}}{(C_{11} - C_{12})(C_{11} + 2C_{12})}, \quad (10)$$

$$S_{12} = \frac{-C_{12}}{(C_{11} - C_{12})(C_{11} + 2C_{12})}, \quad (11)$$

$$S_{44} = \frac{1}{C_{44}}. \quad (12)$$

Based on the Voigt and Reuss bounds, we can estimate the Voigt-Reuss-Hill average, which corresponds to the values for poly-crystalline material⁴. This is given by

$$G_{VRH} = \frac{G_V + G_R}{2}. \quad (13)$$

We use VASPKIT⁵, which implements the above algorithm. Strain values are taken to be -0.004, -0.002, 0.000, 0.002, and 0.004. We use $14 \times 14 \times 14$ k-point mesh for both metals and alloys to estimate energies for G calculation.

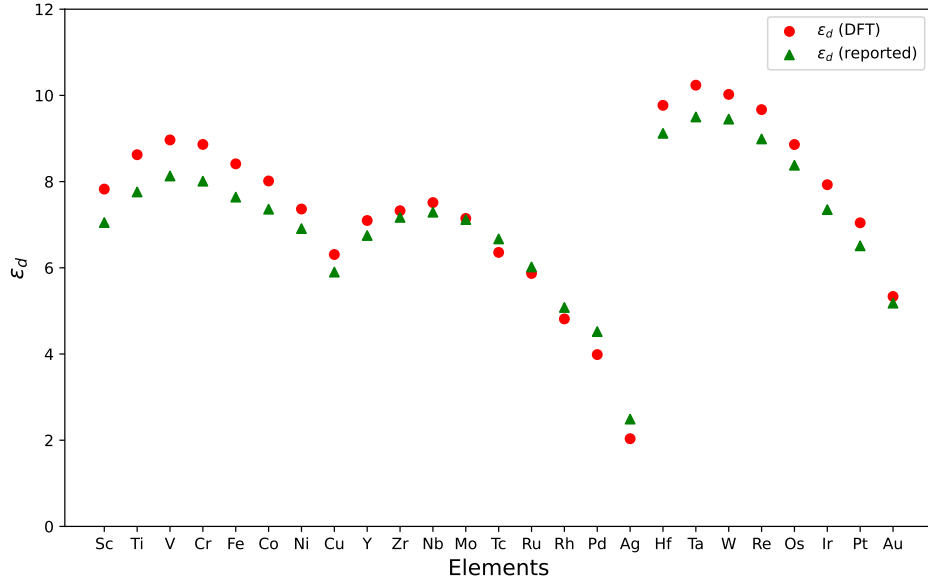


FIG. S1. A comparison of d-band center ϵ_d between reported values⁶ and DFT values for 3d, 4d and 5d elements.

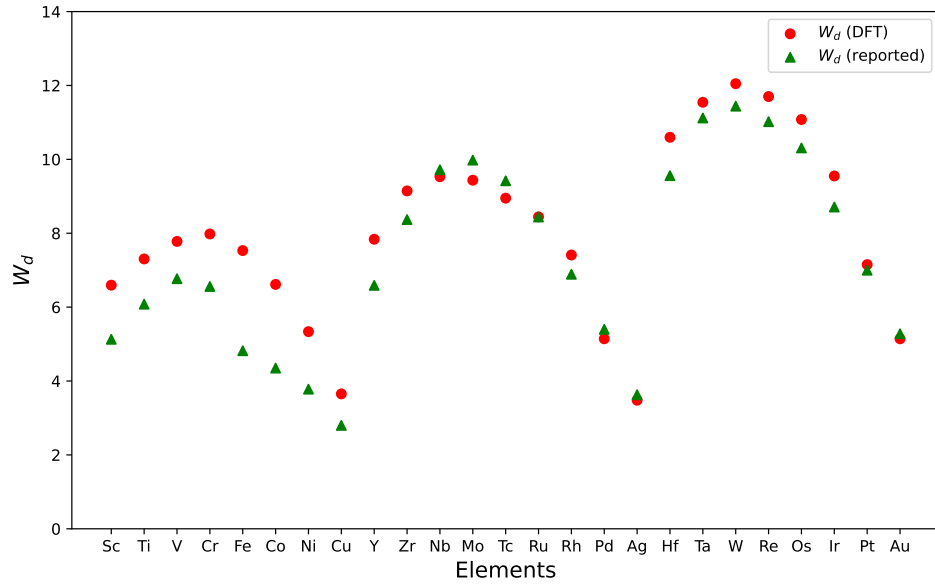


FIG. S2. A comparison of d-band width W_d between reported values⁶ and DFT values for 3d, 4d and 5d elements.

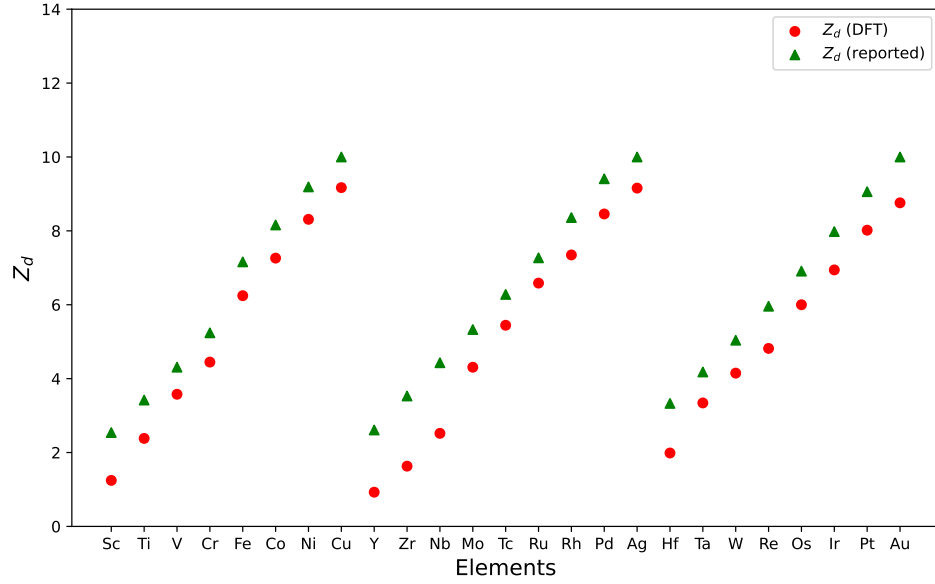


FIG. S3. A comparison of valance d-electrons z_d between reported values⁶ and DFT values for 3d, 4d and 5d elements.

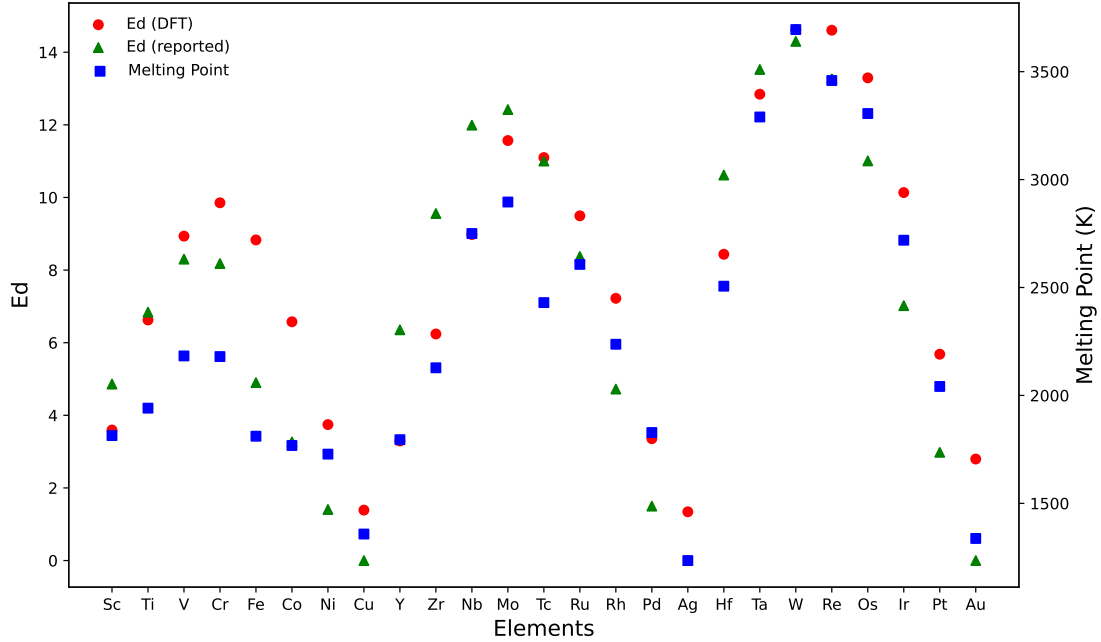


FIG. S4. A comparison of d-electrons cohesive energy E_d between reported values⁶ and DFT values for 3d, 4d and 5d elements. Higher cohesive energy leads to higher melting point (experimental values).

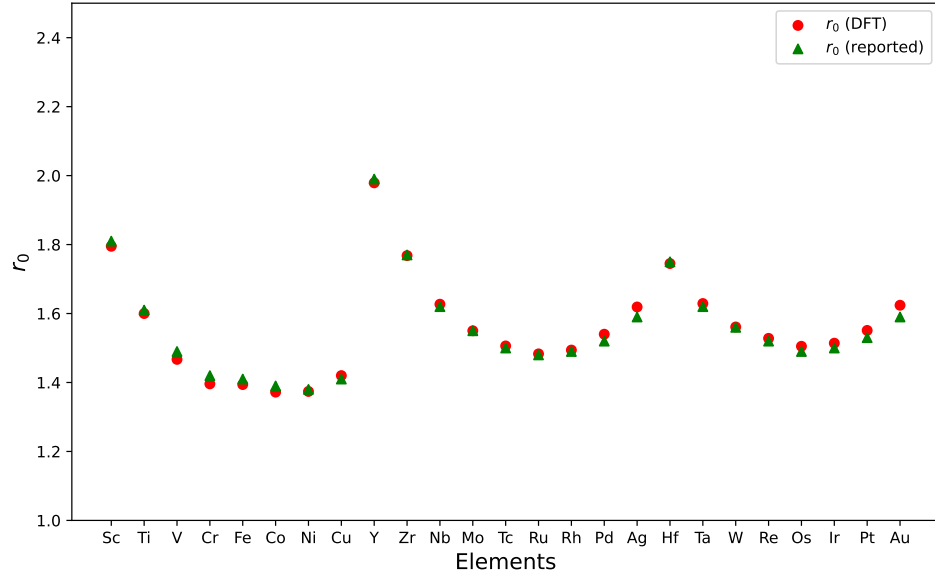


FIG. S5. A comparison of Wigner seitz radius r_o between reported values⁶ and DFT values for 3d, 4d and 5d elements.

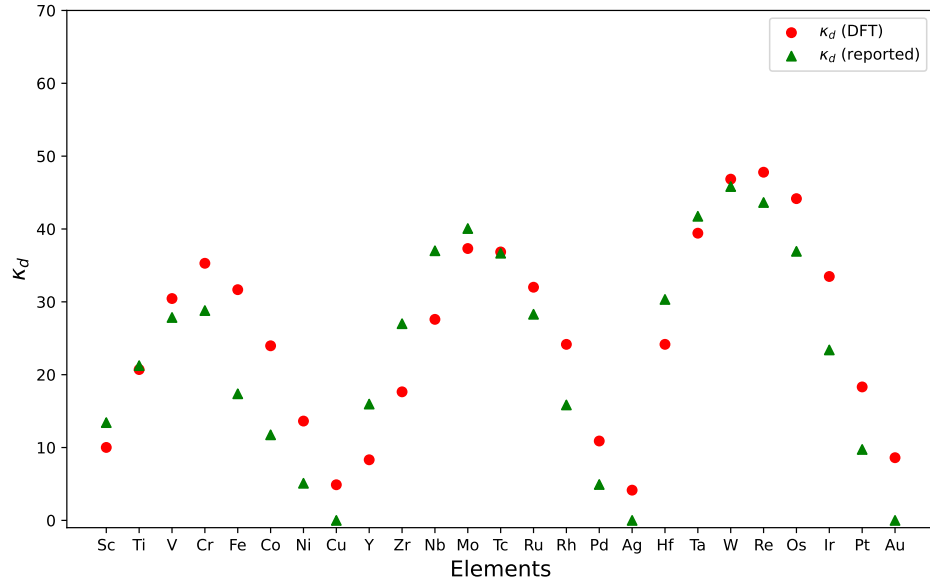


FIG. S6. A comparison of d-electrons bulk modulus κ_d between reported values⁶ and DFT values for 3d, 4d and 5d elements.

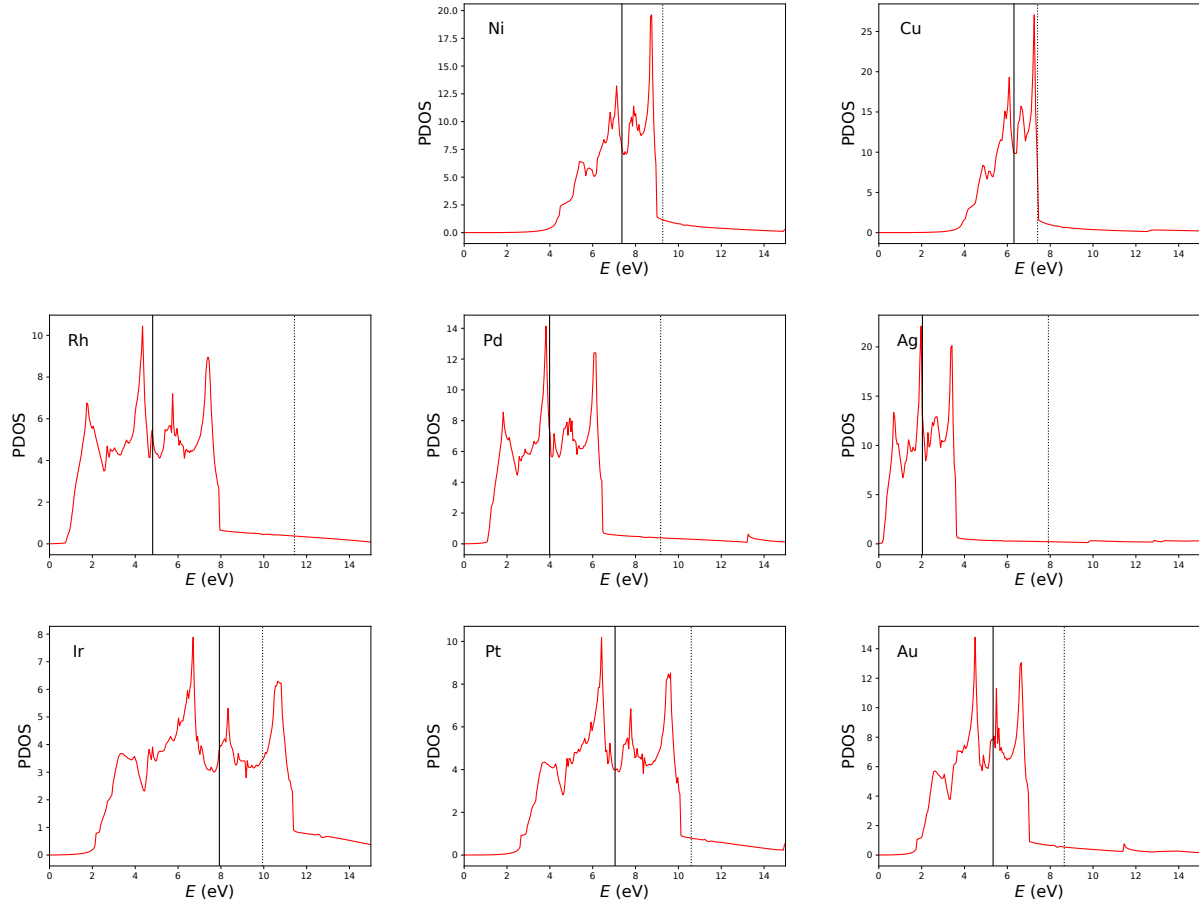


FIG. S7. PDOS of d-orbitals for transition metals of 3d (upper row), 4d (middle row), and 5d (lower row). The solid black line indicates the center of the d-band (ε_d), and the dashed line represents the Fermi energy level (E_F).

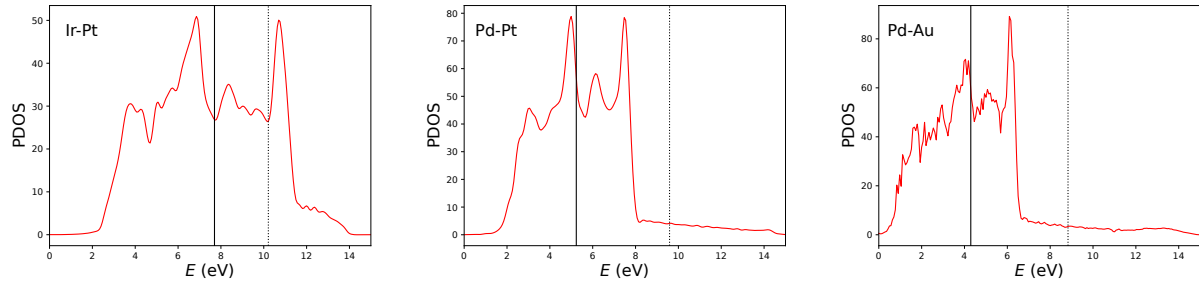


FIG. S8. PDOS plots of d-orbitals for alloys of $\text{Ir}_{0.75}\text{Pt}_{0.25}$, $\text{Pd}_{0.75}\text{Pt}_{0.25}$, and $\text{Pd}_{0.75}\text{Au}_{0.25}$. The solid black line indicates the center of the d-band (ε_d), and the dashed line represents the Fermi energy level (E_F).

II. PREDICTION OF SHEAR MODULUS AND SFE

A. Gaussian Process Regression

Gaussian process regression (GPR) is a robust statistical model designed to learn the underlying function and its associated uncertainty. Gaussian process models estimate uncertainty that increases as one moves away from the training points. This feature quantifies uncertainty when using the surrogate model in future design tasks. To find the best model, we examine and compare three kernels: Radial Basis Function (RBF), Matern, and Exponential. We set RBF to set specific bounds with regulation parameters. An additional parameter is introduced by the Matern kernel, an extension of the RBF, to modify the function's smoothness. The Exponential kernel, which is comparable to the RBF but has a more straightforward shape, is also considered. Finding the best kernel for the model is the goal of the comparison, which considers factors like smoothness, adaptability, and performance in oversampled regions of the space. The Matern kernel produced the best model and the most consistent results out of the three kernels tested for GPRs, with test R^2 of 0.982, 0.992, and 0.992 for G , γ_{ISF} and γ_{ESF} .

B. Support vector regression

Support vector regression (SVR) uses a subset of training data, that is, support vectors, in the final regression model by finding the optimal hyperplane. As a result, SVR models have improved memory efficiency and are less vulnerable to biases in the sampling of the training set. However, using these models makes quantifying uncertainty more difficult. Additionally, we test and compare four kernels, the polynomial, linear, sigmoid, and RBF, to choose the optimum SVR model with the help of grid search cross-validation. SVRs aim to maintain the residuals of all training data below a certain threshold, which lessens the temptation to sacrifice residuals on the minority of data, which results in RBF kernel being less prone to sample biasing and thus gives better results than GPR. The best SVR uses the RBF kernel and is trained with similar data points using Grid Search CV to estimate the best parameters, using which we obtain an R^2 score of 0.984, 0.994, and 0.996 for G , γ_{ISF} and γ_{ESF} .

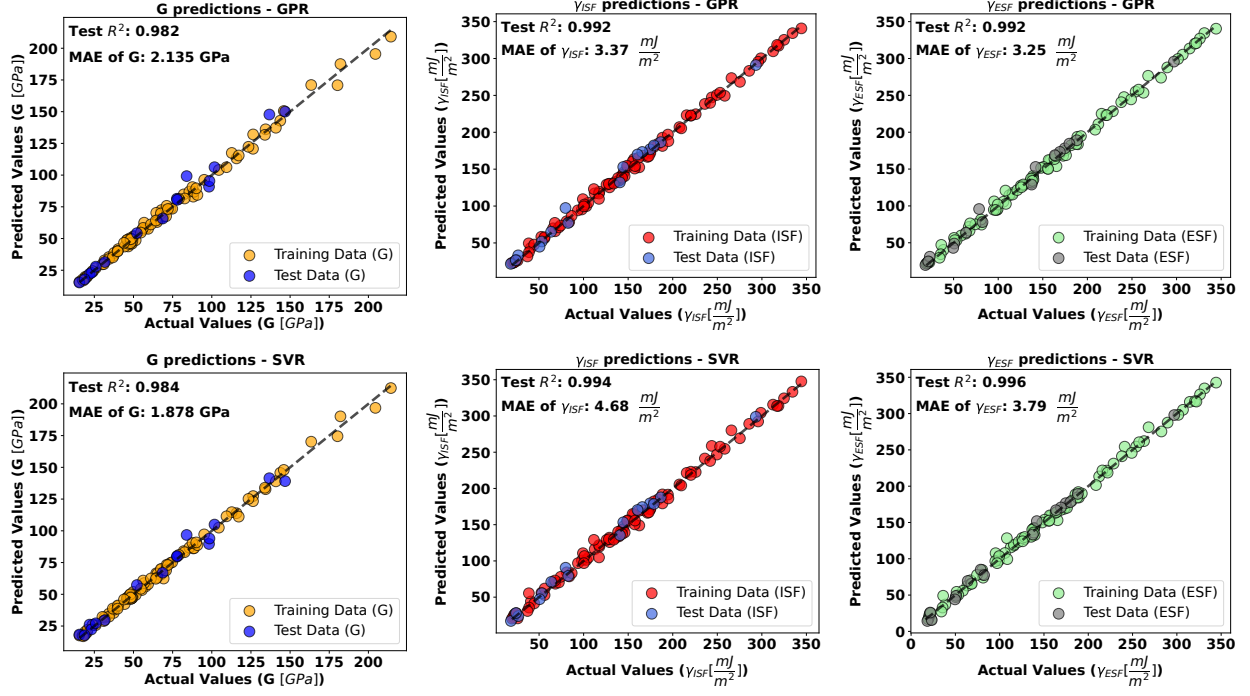


FIG. S9. From left to right, the panels illustrate G , γ_{ISF} , and γ_{ESF} . Top row (Gaussian Process Regression) and bottom row (Support Vector Regression) represents the comparison of predicted vs actual values for training and test datasets.

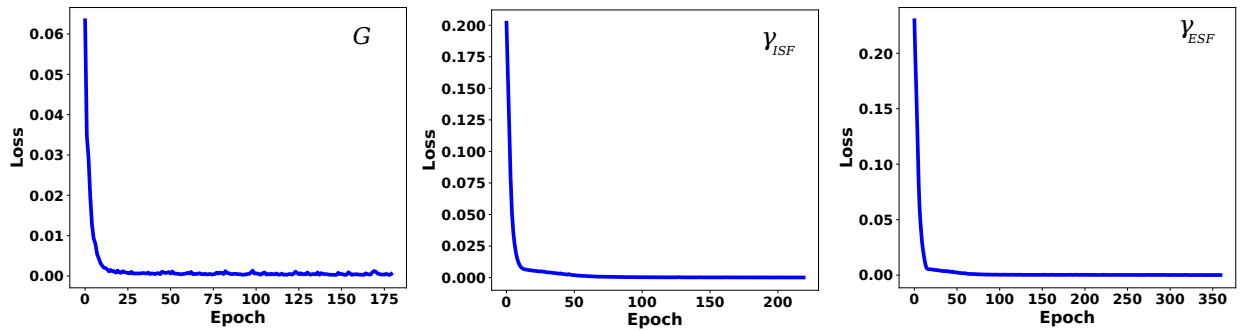


FIG. S10. Epoch vs. loss plots depict the training process of DNNs for G , γ_{ISF} , and γ_{ESF} . The accuracy increases with the number of epochs, reaching a saturation point thereafter.

III. FEATURE IMPORTANCE ANALYSIS

One thousand random trees with a maximum depth ranging from 1 to 100 terms are analyzed to understand the importance of features in a random forest. During the hyperparameter tuning process, we investigate each combination of hyperparameters using Grid-Search Cross-Validation, with different combinations of the number of estimators (random arrangement of parameters) and different maximum depths of branches (selected terms) of random forest trees. Then, we train the model using cross-validation on the different subsets of a combination of randomly selected parameters from the available data to minimize the mean square error of prediction. The feature importance is determined based on the contribution of each feature to the reduction in impurity (reduction in disorder or uncertainty in a data collection attained by decision tree splitting), i.e., minimizing the entropy along with minimizing the mean square error when branches of a random forest tree are split, as quantified by the formula:

$$\text{Importance}(j) = \frac{\sum_t I(j \text{ is used to split in tree } t) \times \text{improvement in impurity}}{\text{Number of trees}}. \quad (14)$$

Here, j represents the index of the feature, which takes the sum of over 1000 trees in the forest. The resulting importance scores provide insights into the relevance of each feature in making accurate predictions. The grid search identifies the best hyperparameters and the features contributing most to the model's accuracy. The selected terms include the first feature with the overall highest feature importance and other features from the decision tree that minimize the total number of terms and mean square error of predicting terms.

* bsomnath@iitk.ac.in

¹ Y. Le Page and P. Saxe, "Symmetry-general least-squares extraction of elastic coefficients from ab initio total energy calculations," Phys. Rev. B, vol. 63, p. 174103, Mar 2001.

² W. Voigt, Lehrbuch der kristallphysik:(mit ausschluss der kristalloptik), vol. 34. BG Teubner, 1910.

³ S. Chandrasekar and S. Santhanam, "A calculation of the bulk modulus of polycrystalline materials," Journal of Materials Science, vol. 24, pp. 4265–4267, Dec 1989.

- ⁴ R. Hill, “The elastic behaviour of a crystalline aggregate,” Proceedings of the Physical Society. Section A, vol. 65, p. 349, may 1952.
- ⁵ V. Wang, N. Xu, J.-C. Liu, G. Tang, and W.-T. Geng, “Vasppkit: A user-friendly interface facilitating high-throughput computing and analysis using vasp code,” Computer Physics Communications, vol. 267, p. 108033, 2021.
- ⁶ W. A. Harrison, Electronic structure and the properties of solids: the physics of the chemical bond. Courier Corporation, 2012.